JPhys Energy

PAPER • OPEN ACCESS

The role of NaSICON surface chemistry in stabilizing fast-charging Na metal solid-state batteries

To cite this article: Edouard Quérel *et al* 2021 *J. Phys. Energy* **3** 044007

IOP Publishing J. Phys. Energy 3 (2021) 044007 https://doi.org/10.1088/2515-7655/ac2fb3

Journal of Physics: Energy

OPEN ACCESS

RECEIVED
13 July 2021

REVISED
30 September 2021

ACCEPTED FOR PUBLICATION
14 October 2021

PUBLISHED
12 November 2021

PAPER

The role of NaSICON surface chemistry in stabilizing fast-charging Na metal solid-state batteries

Edouard Quérel[1,*], Ieuan D Seymour[1], Andrea Cavallaro[1], Qianli Ma[2,*], Frank Tietz[2] and Ainara Aguadero[1,*]

[1] Department of Materials, Imperial College London, London SW7 2AZ, United Kingdom
[2] Forschungszentrum Jülich GmbH, Institute of Energy and Climate Research, Materials Synthesis and Processing (IEK-1), 52425 Jülich, Germany
[*] Authors to whom any correspondence should be addressed.

E-mail: edouard.querel16@imperial.ac.uk, q.ma@fz-juelich.de and a.aguadero@imperial.ac.uk

Keywords: NaSICON, solid state batteries, Na metal, interfaces, XPS, LEIS, DFT, surface energy, interface resistance

Supplementary material for this article is available online

Abstract

Solid-state batteries (SSBs) with alkali metal anodes hold great promise as energetically dense and safe alternatives to conventional Li-ion cells. Whilst, in principle, SSBs have the additional advantage of offering virtually unlimited plating current densities, fast charges have so far only been achieved through sophisticated interface engineering strategies. With a combination of surface sensitive analysis, we reveal that such sophisticated engineering is not necessary in NaSICON solid electrolytes ($Na_{3.4}Zr_2Si_{2.4}P_{0.6}O_{12}$) since optimised performances can be achieved by simple thermal treatments that allow the thermodynamic stabilization of a nanometric Na_3PO_4 protective surface layer. The optimized surface chemistry leads to stabilized Na|NZSP interfaces with exceptionally low interface resistances (down to 0.1 Ω cm^2 at room temperature) and high tolerance to large plating current densities (up to 10 mA cm^{-2}) even for extended cycling periods of 30 min (corresponding to an areal capacity 5 mAh cm^{-2}). The created Na|NZSP interfaces show great stability with increment of only up to 5 Ω cm^2 after four months of cell assembly.

1. Introduction

Increasing the energy density and enhancing the safety of batteries are two notorious objectives motivating the research for new cell chemistries [1, 2]. Replacing conventional carbon anodes by alkali metal ones could offer a significant increase in energy density thanks to the high specific capacity of alkali metals (3860 mAh g^{-1} for Li and 1,166 mAh g^{-1} for Na) and their low redox potential (−3.04 V and −2.71 V versus SHE—standard hydrogen electrode—for Li and Na, respectively). However, to this day, the use of alkali metal anodes in batteries employing liquid electrolytes has been confronted to challenging problems of dendrite growths and low coulombic efficiency [3, 4]. Solid-state batteries (SSBs) featuring solid electrolytes (SEs) theoretically enable the use of alkali metal anodes by making the electrolyte harder to penetrate by dendrites and improve cells' safety by removing the flammability risks associated with organic liquid electrolytes. In addition to electrochemical performance, the environmental impact of new battery chemistries is also being scrutinized as that of Li-ion cells is becoming more and more criticized [5–9]. Sodium based SSBs (Na-SSBs) provide such a sustainable and economical alternative. Furthermore, if the high specific capacity of Li metal could initially make one think that Li-SSBs are more advantageous in terms of gravimetric and volumetric energy density, recent models including all the active and inactive components of a cell indicate that some Na-SSBs could compete with their Li counterparts [10].

Among suitable SEs for Na-SSBs, the family of Na^+ SuperIonic CONductors (NaSICON) of composition $Na_{1+x}Zr_2Si_xP_{3-x}O_{12}$ ($0 \leqslant x \leqslant 3$) has long been recognized for its high ionic conductivity and convenient processability in air [11, 12]. A renewed interest around the synthesis of these materials has recently contributed to enhance their performance to an unprecedented total room temperature conductivity of

5 mS cm^{-1} (15 mS cm^{-1} bulk conductivity) for the $Na_{3.4}Zr_2Si_{2.4}P_{0.6}O_{12}$ composition (further referred to as NZSP) [13]. Improvements in the total ionic conductivity of NaSICON materials were obtained from the optimization of the bulk phase but also, to a large extent, by controlling the densification of these polycrystalline materials which can be promoted by adding a slight off-stoichiometric excess of Na and P during the synthesis [14–17]. Aliovalent substitutions on the Zr site (for instance with Zn^{2+} or Mg^{2+}) have also recently led to NaSICON phases with high ionic conductivity [18, 19].

Although good bulk properties are an essential prerequisite for a material to be considered as a suitable SE, important limitations to the electrochemical performance of SSBs are known to emerge from issues at the anode|SE interface, even more when fast cycling rates are targeted (in the order of several mA cm^{-2}) [20]. Some interrelated challenges affecting the anode|SE interface include: large interface resistances [21]; the coalescence of pores during stripping (discharge) [20, 22]; inhomogeneous plating (charge) with the risk of a short-circuit if the SE is penetrated by alkali metal filaments [23]. Several sophisticated interface engineering strategies have been suggested to solve these problems, such as: improving interfacial wetting by introducing thin alkaliphilic interlayers [24]; the application of large stack pressures to prevent contact loss during cycling [25–27]; and the use of 3D interfaces to increase the surface-active area and mitigate contact loss [28]. Unoptimized Na|NaSICON interfaces are also affected by these issues with, for instance, interface resistances in the kΩ cm^2 range still often reported (see supplementary table 1 (available online at stacks.iop.org/JPENERGY/3/044007/mmedia)).

In this study, we report that a negligible Na|NZSP interface resistance (down to 0.1 Ω cm^2) can be systematically obtained with thermally activated NZSP samples by taking advantage of the *in-situ* stabilization of a Na_3PO_4 layer on their surface upon thermal activation. We demonstrate the existence of this Na_3PO_4 layer using x-ray photoelectron spectroscopy (XPS), low energy ion scattering (LEIS) and first principles calculations based on density functional theory (DFT). This surface layer allows fast-plating rates as revealed by a critical current density (CCD) of 10 mA cm^{-2} and high stability against Na metal.

2. Experimental section

2.1. NZSP synthesis

$Na_{3.4}Zr_2Si_{2.4}P_{0.6}O_{12}$ was synthesized following a solution-assisted solid-state synthesis [13]. $NaNO_3$ (Sigma Aldrich, 99%), $ZrO(NO_3)_2$ (Sigma Aldrich, 99%), $Si(OC_2H_5)_4$ (Sigma Aldrich, 99%) and $NH_4H_2PO_4$ (Sigma Aldrich, 99.5%) were used as starting materials. An off-stoichiometric amount of $NaNO_3$ and $NH_4H_2PO_4$ was added to form an intergranular Na_3PO_4 phase in the ratio $Na_{3.4}Zr_2Si_{2.4}P_{0.6}O_{12}$:1.5%$Na_3PO_4$. The *in-situ* formation of Na_3PO_4 acts as a sinter aid during the synthesis. The optimum ratio of 1.5% was found to yield the best results in terms of phase purity, density and electrochemical performance.

Stoichiometric amounts of $NaNO_3$ and $ZrO(NO_3)_2$ were first dissolved in deionized water. Concentrated HNO_3 was added while stirring to help with the dissolution of precursors. The volume of HNO_3 represented 5% of the total final volume. $Si(OC_2H_5)_4$ was added in stoichiometric proportions and the solution was stirred until complete dissolution of all precursors was observed. Once fully dissolved, the last precursor, $(NH_4)H_2PO_4$, was added to the solution. The addition of $(NH_4)H_2PO_4$ led to the formation of white precipitates. The solution was then homogenized by stirring and dried in a vacuum oven at 80 °C overnight. The dried gel was decomposed at 800 °C for 3 h with a heating and cooling rate of 180 °C h^{-1}. The obtained white powder was ground in an agate mortar and then ball-milled on a roller bench for 72 h in ethanol with zirconia balls. Pellet samples were pressed using a 13 mm diameter die under a load of 1.5 T. Pellets were sintered in Pt crucibles or Al_2O_3 crucibles lined with Pt foil (1285 °C, 6 h, 180 °C h^{-1} heating and cooling rates).

The relative density of NZSP pellets used in this study was estimated geometrically to be 96 ± 2%.

2.2. NZSP surface processing and nomenclature

Pellets were polished with either SiC (Struers, grit sizes: 500, 1200, 2400, 4000). For some samples, ethanol (VWR ethanol absolute >99.8%) was used as a lubricating solvent. To remove surface residues after polishing, pellets were either sonicated in ethanol for 1 min or dusted with compressed air canisters for dry polished samples.

Selected samples were annealed after polishing in a muffle furnace at 900 °C, for 0.5 h with a 900 °C h^{-1} heating and cooling rate. The choice of the annealing temperature and heating/cooling rate was based on previous literature on the Li metal|LLZO interface for which it was demonstrated that a large improvement in interface resistance could be obtained using these annealing parameters [23, 29].

The following nomenclature is used to distinguish the various NZSP samples in the manuscript: ethanol is abbreviated as EtOH; the term 'dry' refers to a polishing condition without solvent; a post-polishing annealing step is indicated by the term 'anneal' in the subscript. For example, $NZSP_{EtOH500\text{-}anneal}$ is an NZSP

pellet which was polished with SiC paper of grit size 500, using ethanol as solvent, followed by an annealing step at 900 °C. $NZSP_{\text{as sintered}}$ refers to samples which were neither polished nor annealed. Finally, $NZSP_{\text{Xsection}}$ refers to a sample which was snapped in half to analyze the chemical composition of the center of a pellet.

2.3. NZSP structure and microstructure characterization

The crystal structure and purity of NZSP samples were tested by x-ray diffraction (XRD) on a PANalytical MPD powder diffractometer with monochromatic Cu $K_{\alpha 1}$ radiation ($\lambda = 1.540\,598$ Å). Patterns were collected in a 2θ range between 10 and 80° with a step size of 0.033° and a 3 s collection time at each step. The crystalline structure of NZSP samples was analyzed by XRD. X-ray diffractograms are presented in supplementary figure 1. The reader is referred to a previous publication for details on the NZSP crystal structure [13].

SEM images were obtained using the in-lens detector of a Zeiss Leo Gemini 1525 at a working distance of 7 mm with an electron beam accelerating voltage of 5 kV and a 30 μm aperture. EDX spectra were measured with an Oxford Instrument x-act detector using the same beam excitation. A low accelerating voltage was chosen to ensure a reduced interaction volume and higher surface sensitivity. The low x-ray production rate was compensated by longer integration times.

2.4. Cell assembly

Na metal films were freshly prepared for each assembled cell in an Ar-filled glovebox. A clean piece of Na was cut from a rod (Na sticks, covered in film of protective hydrocarbon oil, 99%, Alfa Aesar), then pressed flat in a LDPE plastic bag to a thickness of 100–300 μm. Circular electrodes were then punched from this foil. Their surface was mechanically cleaned using the blade of a scalpel. The Na metal electrodes were then placed on both sides of a NZSP pellet and the Na|NZSP|Na stack was pressed with a uniaxial pressure of around 10 MPa. The applied pressure was measured using a KMM50-10 kN force sensor (inelta Sensorsysteme GmbH). The diameter of the Na metal electrodes was measured after the cell was pressed. For electrochemical tests requiring instruments outside the glovebox, the symmetrical cells were placed in stainless steel coin cells.

2.5. Electrochemical measurements

Impedance spectra were measured on a Solartron 1260 and a Biologic VMP-300 frequency response analyzers (FRAs) with an excitation amplitude of $V_{\text{A.C.}} = 50$ mV. For the Solartron measurements, data points were collected in the frequency range of 13 MHz to 5 Hz (7 MHz to 1 Hz for the Biologic) with a logarithmic sampling at 20 points/decade. To minimize the signal to noise ratio, the frequency range was split into three sub-ranges (13 MHz–500 kHz, 500 kHz–500 Hz, 500 Hz–5 Hz) with varying integration times and delays (2 s integration and ten cycles delay; 1 sec integration and five cycles delay; 30 cycles integration and three cycles delay, respectively). The temperature was maintained at 25 °C using a Linkam HFS600 E-P temperature control stage. Results were fitted using RelaxIS3 (Rhd instruments). The reported capacitance values were calculated using the Brug formula:

$$C = \frac{(Q * R)^{1/n}}{R}$$

where Q and n are the parameters of the Constant Phase Elements used in the equivalent circuit models.

As impedance spectra were measured on two different FRAs, a difference in the systems' ohmic resistances was noticed. For samples measured on the instrument with higher ohmic resistance, the spectra were shifted so that the high frequency intercept with the real axis corresponds to a bulk conductivity of 15 mS cm^{-1} (as previously measured). [13]

The CCD of Na|NZSP|Na symmetric cells was tested using a Scribner 580 battery cycler. Cells were typically cycled between 0.5 mA cm^{-2} and 15 mA cm^{-2} until signs of a short-circuit were observed. Depending on the measurement, either the cycled capacity or the duration of the galvanostatic dwell were kept constant. Formation cycles consists in a simultaneous stepwise increase of the cycling current density (from 1 to 10 mA cm^{-2}) and dwell time (from 30 s to 0.5 h).

2.6. X-ray photoelectron spectroscopy (XPS)

XPS spectra were collected at room temperature on a Thermo Fisher Scientific XPS system with a monochromated Al K_{α} source (1486.6 eV) operating at a 2×10^{-9} mbar base pressure. The x-ray source was operated at 6 mA emission current and 12 kV anode bias providing a 400 μm^2 x-ray spot size. Core level spectra were measured using a pass energy of 20 eV, at a resolution of 0.1 eV and an integration time of 50 ms/point. Averages over a number of scans varying from 30 for intense signals (Na1s for instance) to 80 for lower intensity signals (P2p) were taken. Sample charging was neutralized using a low energy electron flood gun (0.2 V, 100 μA). Results were fitted using the Avantage software (Thermo Fisher Scientific). The

background was fitted using a modified Shirley type function which includes a condition of non-intersection between the background and the data points. The Zr3d5 peak position was used as a reference for charge compensation (Zr3d5 fixed at 182.40 eV) and intensity normalization.

A vacuum suitcase (Thermo Fisher Scientific XPS Vacuum Transfer Module) was used for the transport of air sensitive samples (such as Na metal) from a glovebox to the XPS chamber to minimize contaminations originating from the transfer. For this purpose, the vacuum suitcase was left under active vacuum for 12 h to desorb molecules from its surface before the Na metal was placed on the sample holder.

2.7. Low energy ion scattering (LEIS)

The LEIS analysis was carried out in an Ion-ToF Qtac100 instrument by ION-TOF GmbH. The Qtac energy analyzer is extremely surface sensitive providing quantitative elemental characterization of the first atomic layer of the sample. The base pressure in the analysis chamber was $\sim 9 \times 10^{-10}$ mbar. During the experiment, the chamber pressure increases to 10^{-8} mbar because of the noble gas flux from the ion source. For the measurements, a 3 keV $^4He^+$ ion beam was used. A He^+ ion source was chosen because of its high sensitivity to low mass atoms. The primary ion beam was aligned perpendicular to the samples' surface and the scattered ions were detected at an angle of 145°. The primary ion beam was scanned on a sample surface area of 500×500 μm. To prevent charging effects due to the insulating nature of NaSICON samples, a low-energy electron flood gun (10 eV) was used.

The energy of each peak position can be calculated according to the laws of conservation of energy and momentum [30]. The primary ions that overcome the first atomic layer are mostly neutralized. The ones that are both scattered from deeper sample layers and re-ionized by the interaction with the oxide surface lead to an in-depth signal, which appears in the spectra as a left background shoulder with respect to the elastic atomic peak position. More details about the technique can be found elsewhere [31].

With this study, a preferential sputtering of Na atoms (even at a low sputtering energy of 0.5 keV) was noticed. As the ion dose increases the sodium signal decreases. Sodium depletion from Ar^+-bombarded silicate glass surfaces has already been reported [32]. For this reason, the area of the Na peak was not used in the normalized results. More specifically, the normalized results were obtained by dividing the area of each peak (obtained by curve fitting) to the total area of all detectable peaks.

2.8. First principles calculations

DFT calculations of end member $NaZr_2P_3O_{12}$ (NZP) and $Na_4Zr_2Si_3O_{12}$ (NZS) NaSICON compositions were performed with the Vienna *ab initio* simulation package (VASP), using the Perdew–Burke–Ernzerhof exchange-correlation functional [33, 34]. Projector-augmented wave (PAW) pseudopotentials were used for all species, with a plane wave cut off of 500 eV [35]. To minimize the computational cost, the softest PAW pseudopotentials from each element were used from the VASP 5.4.4 distribution, which are labelled Na, Zr_sv, P, Si and O_s. Tests using pseudopotentials containing additional valence electrons did not result in qualitative differences to the surface energies or structures. An energy convergence of 1×10^{-6} eV or better was used for all calculations and spin polarization was included unless otherwise stated. A gamma-centered k-point mesh with mesh density of 20 Å or better was used to sample the Brillouin zone, unless otherwise stated. The primitive, bulk unit cell structures of NZP and NZS ($R\bar{3}m$) were fully optimized without symmetry constraints until the force on any atom fell below 0.01 eV $Å^{-1}$.

The reader is referred to the SI for more information about surface creation and surface energy calculations.

3. Results

3.1. The processing of NZSP surfaces impacts the Na|NZSP interface resistance

To evaluate how the NZSP surface processing influences the electrochemical performances of Na|NZSP interfaces, impedance spectra of three types of Na|NZSP|Na symmetrical cells are compared. The surface of NZSP pellets used for these cells are either unaltered after sintering ($NZSP_{\text{as sintered}}$), roughly polished with ethanol as solvent ($NZSP_{\text{EtOH500}}$), or polished and annealed ($NZSP_{\text{EtOH500-anneal}}$). For more information about the samples' nomenclature, the reader is referred to the experimental section (section 2). Normalized Nyquist plots representing the impedance spectra of the three symmetrical cells are presented in figure 1. The models used for equivalent circuit fitting are included in inset and consist of a resistor R_{HF} (high frequency resistance), an inductor L (accounting for high frequency inductive effects from the measurement setup), and either one or two R-CPE elements (CPE: constant phase element) depending on the number of observed semi-circles. The calculated fitting parameters can be found in table S3.

Detecting the bulk diffusion of Na^+ ions through the NSZP structure is not possible at room temperature in the frequency range covered by the FRAs used in this study [13]. In the equivalent circuits,

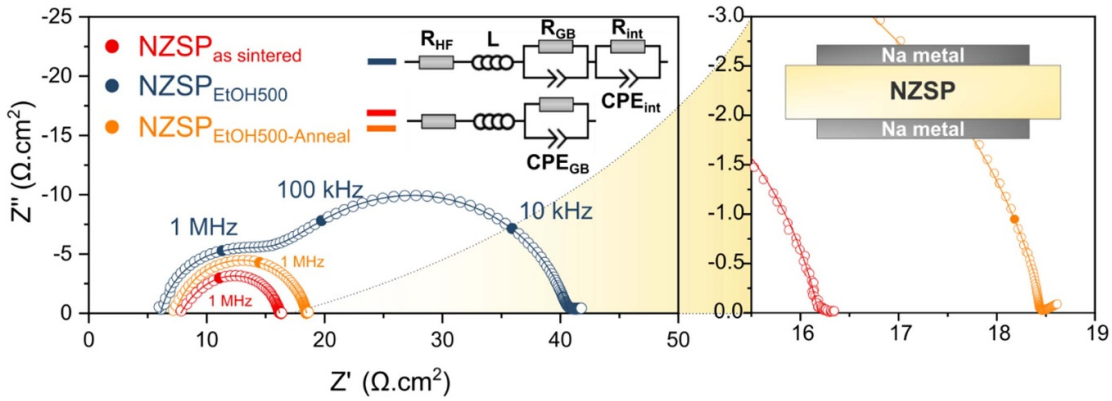

Figure 1. The processing of NZSP surfaces impacts the Na|NZSP interface resistance. Nyquist plots of Na|NZSP|Na symmetrical cells ($NZSP_{as\ sintered}$, $NZSP_{EtOH500}$ and $NZSP_{EtOH500\text{-}anneal}$). Data points are shown as open circles, frequency markers are shown as filled circles, and the respective fits (obtained with the equivalent circuits shown in inset) are represented as a solid line. The data presented are normalized to the area of the electrodes and divided by two.

R_{HF} therefore accounts for the resistive contributions of the bulk diffusion with the ohmic losses of the impedance analyzer. For all three samples, the semi-circle observed at high frequency (with an apex at a frequency of around 1 MHz and capacitance of $C_{GB} \approx 3\text{–}5 \times 10^{-9}$ F) can be attributed to grain boundary diffusion, as was already demonstrated in previous literature and confirmed here with the impedance results of a Au|NZSP|Au symmetrical cell (see supplementary figure 2) [13, 36].

A second semi-circle attributed to the transfer of Na^+ ions across the Na|NZSP interface (modelled by R_{int} and CPE_{int}, equivalent capacitance $C_{int} = 6.99 \times 10^{-7}$ F) can be clearly observed for the $NZSP_{EtOH500}$ sample. The calculated interface resistance of 24.2 Ω cm^2 is quite low in comparison to other studies reported in table S1. As an interface semi-circle is not distinguishable for the $NZSP_{as\ sintered}$ and $NZSP_{EtOH500\text{-}anneal}$ samples, their interface resistances were estimated using the procedure described by Krauskopf *et al* [37] by calculating the difference between $Z'_{data}(f_{min})$ and Z'_{fit} ($f \rightarrow 0$ Hz). This results in interfacial resistances as low as 0.2 and 0.1 Ω cm^2 for the $NZSP_{as\ sintered}$ and $NZSP_{EtOH500\text{-}anneal}$ samples, respectively.

To rule out a possible influence of the polishing medium in the larger interface resistance of $NZSP_{EtOH500}$, another set of symmetrical cells were assembled from dry polished samples ($NZSP_{dry500}$). The interface resistance calculated from the $NZSP_{dry500}$ cell presented in supplementary figure 3 (22.1 Ω cm^2) is equivalent to $NZSP_{EtOH500}$, indicating that the use of a polishing solvent has no influence on the Na|NZSP interface resistance.

A much more significant impact on the Na|NZSP interface resistance is observed when NZSP samples are finely polished, either with a solvent ($NZSP_{EtOH4000}$) or without a solvent ($NZSP_{dry4000}$). In this case, as illustrated in supplementary figures 3 and 4, interface resistances in the range of 4–9 kΩ cm^2 are obtained. Yet, even if NZSP samples are finely polished, a thermal annealing can restore a negligible Na|NZSP interface resistance (see supplementary figures 3 and 4).

These results demonstrate that the Na|NZSP interface resistance depends on the processing conditions of the NZSP surface. Thermally activated NZSP surfaces yield the best electrochemical performance. The detrimental effect of polishing NZSP surfaces on the Na|NZSP interface resistance can be cancelled by annealing.

3.2. Comparison of the surface chemistry of NZSP samples by XPS

To elucidate the origin of the good electrochemical performance of cells employing thermally activated NZSP pellets, the surface composition of NZSP samples were first analyzed by XPS. Figure 2 compares the signals of three NZSP core levels (Na 1s, P 2p and C 1s) for three samples ($NZSP_{as\ sintered}$, $NZSP_{EtOH500}$ and $NZSP_{EtOH500\text{-}anneal}$). To ease the comparison of relative elemental intensities between samples, it is convenient to consider the concentration of one element in the NZSP phase to be fixed. Here, the Zr concentration in the NZSP phase was chosen as the normalization constant over that of Si and P because variations in the surface concentration of Si and P cannot be excluded considering these elements have partial occupancies of the same crystallographic position. More precisely, the signals were normalized so that the $Zr3d_{5/2}$ peak area of all samples were equal (see figure S6). Survey spectra and other core level spectra can be found in supplementary figures 5 and 6.

C1s spectra were collected for each sample to monitor the impact of polishing and thermal treatments on surface carbon contamination. Adventitious carbon species are present on essentially all surfaces exposed to

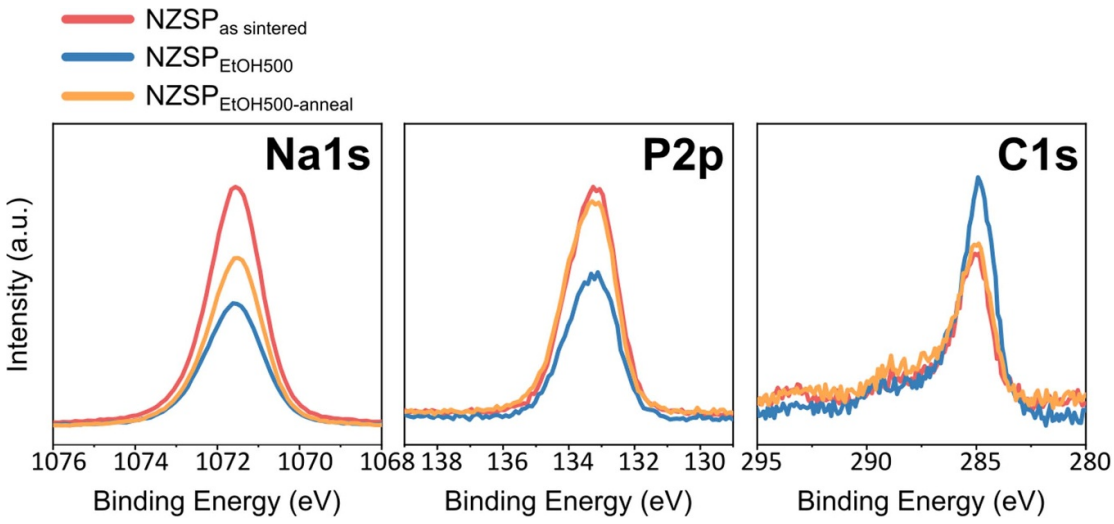

Figure 2. Comparison of the surface chemistry of NZSP samples by XPS. Core level XPS spectra of samples $NZSP_{as\ sintered}$, $NZSP_{EtOH500}$ and $NZSP_{EtOH500\text{-}anneal}$. (charge correction: Zr3d5/2 at 182.4 eV; intensity normalization between samples: Zr3d5/2 peak area).

ambient air and are a common feature observed in XPS spectra [38]. In addition to ambient air contamination, polishing samples can also impact their surface composition. In recent studies, polished surfaces of various SEs were demonstrated to be composed of carbonate or hydroxide species [21, 39]. Poor ionic transport across metal|SE interfaces is often observed when SE surfaces are covered with adventitious species [21, 39–41]. For NZSP, the presence of numerous overlapping peaks in the O 1s signal makes the identification of hydroxide species arduous, therefore the C1s signal is used here as a descriptor for the extent of surface contamination.

Figure 2 reveals that NZSP samples, whichever surface processing they have received, have a similarly low level of surface carbon contamination (around 4 at.% of the total surface signal). The only exception is for the finely polished NZSP samples ($NZSP_{EtOH4000}$ and $NZSP_{dry4000}$) for which a higher level of C contamination was detected (see supplementary figures 7 and 8).

As can be seen from figure 2, the Na1s and P2p signals of the thermally activated samples ($NZSP_{as\ sintered}$ and $NZSP_{EtOH500\text{-}anneal}$) have much larger peak areas in comparison to the polished sample ($NZSP_{EtOH500}$). This difference in peak areas reflects changes in the surface atomic concentrations between samples. More precisely, since the peak intensities were normalized to the Zr3d5/2 peak area, a higher intensity of the Na1s and P2p signals means that the Na:Zr and P:Zr surface atomic ratios of the thermally activated samples are larger than that of the polished sample. These results either suggest that: (a) the Na and P concentrations in the NZSP phase are simultaneously increasing, or that (b) a secondary phase rich in Na and P exists at the surface of thermally activated samples. For hypothesis (1), an increase of the P concentration in the NZSP phase could be explained by a depth-dependent rearrangement of Si and P atoms (with a higher concentration of P towards the sample surface in comparison to the bulk). As a reminder, the original NZSP compositional space is described by the general stoichiometry $Na_{1+x}Zr_2Si_xP_{3-x}O_{12}$ [11]; a substitution of Si by P atoms should therefore result in a lower Na concentration to respect charge balance. The fact that an increase in the Na concentration is observed either suggests that hypothesis (1) is incorrect, or that another charge compensation mechanism is involved (for instance with O vacancies). The experimental results presented in the following sections suggest that hypothesis (2) is correct and explain the XPS results better.

The higher Na and P concentration on the thermally activated NZSP surfaces is also verified with finely polished samples as illustrated in supplementary figure 7. Here again, the thermally activated sample ($NZSP_{EtOH4000\text{-}anneal}$), which was characterized by a low interface resistance, has more intense Na 1s and P 2p signals than the polished sample ($NZSP_{EtOH4000}$).

3.3. LEIS reveals the surface composition of thermally activated NZSP

To confirm the composition and determine the coverage of the surface layer whose existence was suggested by XPS, LEIS was employed. LEIS relies on the binary collision between low energy primary ions (here He^+ ions) and the elements present on the surface of a specimen. A LEIS instrument collects the He^+ ions scattered by a surface at an optimum angle defined by the LEIS detector. The position of the peaks observed in the LEIS energy spectra depends on the primary ions mass, the primary ions energy, the mass of the

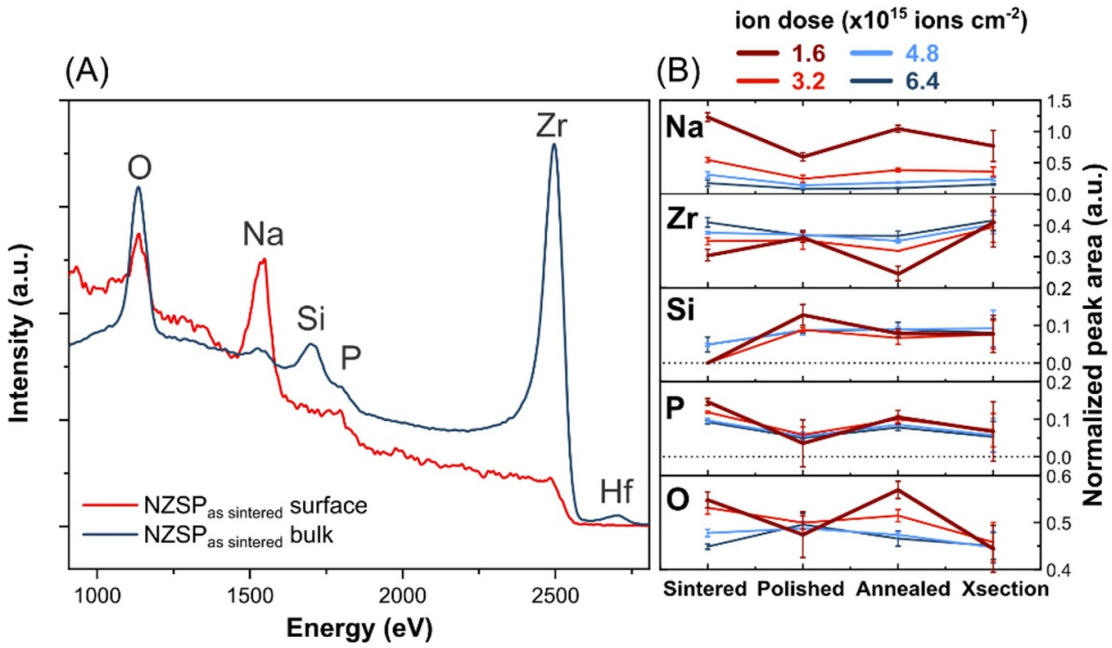

Figure 3. LEIS reveals the surface composition of thermally activated NZSP. (A) $^4He^+$ ion LEIS energy spectra of a $NZSP_{as\ sintered}$ sample comparing the signal of its first atomic layer (for a 8×10^{14} ions cm^{-2} dose, in red) to its average bulk signal (in blue), (B) Comparison of the normalized LEIS peak areas of four NZSP samples with increasing ion doses ('Sintered' = $NZSP_{as\ sintered}$, 'Polished' = $NZSP_{EtOH4000}$, 'Annealed' = $NZSP_{EtOH4000\text{-}anneal}$, 'Xsection' = $NZSP_{cross\text{-}section}$). Each point is the average of three peak areas measured on three different points on the surface of each sample. Error bars correspond to standard deviations.

analyzed atomic species and the detector acceptance angle. To simplify the syntax in the following paragraphs, the peaks will be named according to the analyzed interacting element (e.g. 'the Na peak') although it should be understood as scattered He^+ ions which interacted with the respective surface atom. As the method employs low energy and low mass primary ions, LEIS is a non-destructive technique able to measure the chemical composition of the uppermost atomic layer of the specimen (supplementary figure 9). In practice, as with any ion analysis technique, some partial sputtering of surface atoms will occur and is a function of the primary ion dose exposure. For all the LEIS analyses, the He^+ ion primary beam was scanned on a large area of $500 \times 500\ \mu m$. The surface composition determined by LEIS is an average composition of this entire area.

Two LEIS energy spectra corresponding to the surface (in red) and the bulk (in blue) composition of a $NZSP_{as\ sintered}$ sample are presented in figure 3(a). The surface spectrum was collected with a He^+ ion dose of 8×10^{14} ions cm^{-2}. After having collected this surface spectrum, an Ar^+ ion sputtering beam was used to reveal deeper layers of the sample. At regular intervals, the Ar^+ sputtering beam was alternated with the He^+ ion analysis beam to obtain a depth profile. The averaged signal of all the spectra collected during this depth profile is the bulk spectrum in figure 3(a). The LEIS energy spectrum of the $NZSP_{as\ sintered}$ first atomic layer indicates that it is only constituted of Na, P and O atoms. Zr and Si do not appear on the surface of $NZSP_{as\ sintered}$. In contrast, the averaged depth profile LEIS energy spectrum (in blue) shows that O, Na, Si, P and Zr are present underneath a thin surface layer. Regarding the Na peak, the surface of $NZSP_{as\ sintered}$ samples seems to be enriched in sodium in comparison to its bulk. In reality, the low intensity of the Na peak in the bulk spectrum is associated to a challenging issue of preferential sputtering (see experimental section for more details section (2)). Overall, the LEIS spectra suggest that the entire surface of $NZSP_{as\ sintered}$ is terminated by Na, P and O atoms. The presence of a Zr in-depth signal around 2500 eV in the LEIS energy spectrum of the first atomic layer (see experimental section for more details (section 2)) indicates that the sodium phosphate surface layer must be extremely thin.

In figure 3(b), the surface composition of $NZSP_{as\ sintered}$ is compared with the composition of a polished ($NZSP_{EtOH4000}$) and a polished and annealed ($NZSP_{EtOH4000\text{-}anneal}$) sample. A fresh cleaved NZSP sample (cross-section of a pellet) was also analyzed. This measurement provided information about the bulk composition of NZSP samples. For each sample, LEIS spectra were collected on three different areas. On each area, four consecutive measurements were collected. A schematic illustrating the sequential LEIS analysis is presented in supplementary figure 10. In figure 3(b), the averaged Na, Zr, Si, P and O peak normalized intensities are plotted as a function of the He^+ primary ion dose. Details about the normalization procedure can be found in the experimental section (section 2).

Table 1. DFT computed surface energies for selected $NaZr_2P_3O_{12}$ and $Na_4Zr_2Si_3O_{12}$ surfaces. The surface energies for both stoichiometric and Na_3PO_4 capped $(1\bar{1}02)$ surfaces are given.

	Surface energy ($J\ m^{-2}$)			
	$NaZr_2P_3O_{12}$		$Na_4Zr_2Si_3O_{12}$	
Plane	Bare	Na_3PO_4 terminated	Bare	Na_3PO_4 terminated
$(1\bar{1}02)$	0.69	0.44	0.67	0.58
$(10\bar{1}4)$	0.86	—	0.88	—
$(11\bar{2}0)$	1.15	—	1.26	—
(0003)	0.97	—	0.89	—

Figure 3(b) can be used to compare, the surface composition of the different NZSP samples at a given ion dose. The largest differences can be found for the lowest He^+ ion dose (1.6×10^{15} ions cm^{-2}, shown in dark red). Thermally activated NZSP samples have more Na and P on their surface than polished samples. The Na and P normalized peak areas of $NZSP_{\text{as sintered}}$ are more than twice as high as the $NZSP_{\text{EtOH4000}}$ sample. More importantly, the signal corresponding to Si cannot be initially detected on the surface of $NZSP_{\text{as sintered}}$ samples and only appears after a cumulated ion dose of 4.8×10^{15} ions cm^{-2}.

Figure 3(b) also shows that the surface composition of thermally activated samples is more impacted by the received ion dose than the polished sample. As the ion dose increases from 1.6 to 6.4×10^{15} ions cm^{-2} and deeper atomic layers are slowly revealed, differences in the surface chemical composition of samples attenuate. Taking $NZSP_{\text{as sintered}}$ as an example, the intensity of the P peak attenuates with an increasing ion dose, while simultaneously the intensity of the Zr and Si peaks increases. Variations in the intensity of the Na peak are not related to changes in composition but rather to the previously mentioned problem of preferential sputtering; this explains why the intensity of the Na peak decreases for all samples with higher ion doses. In comparison to $NZSP_{\text{as sintered}}$, the composition of $NZSP_{\text{EtOH4000}}$ does not significantly change with an increasing ion dose and stays within its error bars. This suggest that the Na_3PO_4 layer on the surface of thermally activated NZSP samples is only a few nanometers thick. By removing this surface layer with a low ion dose, a surface composition close to that of a polished sample is obtained. LEIS shows that the entire NZSP surface is covered by a thin Na_3PO_4 layer. Locally, this layer was also observed to be thicker by scanning electron microscopy (supplementary note 1, supplementary figures 11–14).

In agreement with our XPS results, our LEIS analysis confirms that thermally activated samples stabilize a very thin sodium phosphate layer on their surface.

3.4. DFT calculations predict a lower surface energy for Na_3PO_4 terminated NZS/NZP

As our experimental results converge to the conclusion that the thermal activation of NZSP samples results in the stabilization of a sodium phosphate surface, we used DFT calculations to understand the thermodynamic driving force for this process. The aim of this section is to compare the energies of Na_xP_yO terminated NaSICON surfaces with that of bare NaSICON surfaces.

In the absence of an extensive DFT literature on the $Na_{1+x}Zr_2Si_xP_{3-x}O_{12}$ $(0 \leqslant x \leqslant 3)$ family of materials, a first necessary step was to identify the NZSP surfaces with lowest energy (i.e. the most likely to form experimentally). A decision was made to focus on the two end member compositions $NaZr_2P_3O_{12}$ (NZP) and $Na_4Zr_2Si_3O_{12}$ (NZS) to remove the complexity of handling partial occupancies in the Si/P site. The surface energies and structures of the $(1\bar{1}02)$, (0003), $(11\bar{2}0)$ and $(10\bar{1}4)$ planes of NZP and NZS are shown in table 1, supplementary table 3 and supplementary figure 15.

Previous studies of phosphates and oxides have demonstrated that the cleavage of transition metal-O bonds results in high energy surfaces [42, 43]. For NZP and NZS, the $(1\bar{1}02)$ surface has the lowest energy, which is consistent with the fivefold coordination of Zr (ZrO_5) on the surface in comparison to the $(10\bar{1}4)$ and (0003), planes with four- and threefold coordinated Zr, respectively. The $(11\bar{2}0)$ surface, which also has fivefold coordinated Zr on the surface, has a higher surface energy than the $(1\bar{1}02)$ plane as the surface PO_4/SiO_4 groups have a lower coordination with neighboring Na^+ ions. Although only a limited number of surface terminations have been investigated in this study, the significantly lower energy of the $\{1\bar{1}02\}$ family of planes relative to other surfaces for NZP/NZS would result in an approximately cubic morphology from a Wulff construction (figure 4), which is consistent with the cubic morphology of grains observed experimentally in this work and analogous NaSICON materials in other studies [44, 45].

It can be seen from tables 1 and S4 that the $(1\bar{1}02)$ planes of NZP and NZS have similar surface energies ($0.69\ J\ m^{-2}$ and $0.67\ J\ m^{-2}$, respectively), even though the latter surface contains a larger number of undercoordinated Na^+ ions. The similarity between the different materials suggests that the nature of the tetrahedral Si^{4+} or P^{5+} ion has less of an impact on the surface energy than the coordination of the Zr^{4+} ion.

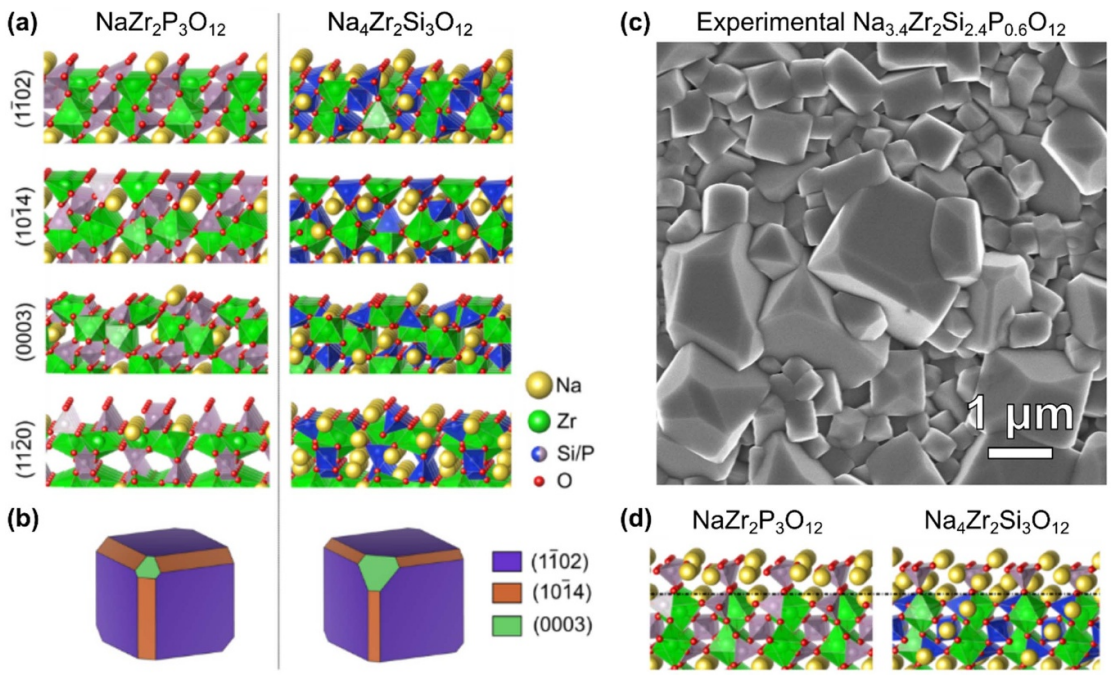

Figure 4. Surface energy DFT calculations of Na_3PO_4 terminated NZS/NZP. (A) DFT optimized surface structures and (B) Wulff energy plot for selected stoichiometric $NaZr_2P_3O_{12}$ and $Na_4Zr_2Si_3O_{12}$ surfaces. (C) SEM image of $Na_{3.4}Zr_2Si_{2.4}P_{0.6}O_{12}$ showing corresponding cube like grain morphology. (D) DFT optimized $NaZr_2P_3O_{12}$ and $Na_4Zr_2Si_3O_{12}$ $(1\bar{1}02)$ surfaces capped with a monolayer of Na_3PO_4. The termination plane of the original stoichiometric (uncapped) surface is indicated with a black dashed line.

Following these preliminary calculations, the influence of a surface Na_3PO_4 film on the surface energy of $Na_{1+x}Zr_2Si_xP_{3-x}O_{12}$ phases could be investigated by adding a single layer of Na_3PO_4 to the low energy $(1\bar{1}02)$ surfaces of NZP and NZS. The specific Na_3PO_4 phosphate composition was selected because it is the predicted decomposition product from thermodynamic analysis using energetics from the Materials Project [46]. For the composition of $Na_{3.4}Zr_2Si_{2.4}P_{0.6}O_{12}$ under study in this work:

$$Na_{3.4}Zr_2Si_{2.4}P_{0.6}O_{12} \rightarrow 0.4\ Na_3Zr_2Si_2PO_{12} + 0.8\ Na_2ZrSi_2O_7 + 0.2\ Na_3PO_4 + 0.4\ ZrO_2. \quad (1)$$

A short (4 ps) *ab initio* molecular dynamics run at 500 K was used to equilibrate the surface atomic positions, followed by structural optimization. The resulting surfaces are shown in figure 4. For both materials, the PO_4 groups in the Na_3PO_4 layer are bound to the fivefold coordinated Zr sites on the surfaces, resulting in a stable ZrO_6 octahedron. From table 1, it can be seen that the surface energy of the Na_3PO_4 capped NZP and NZS $(1\bar{1}02)$ surfaces is lower than the corresponding bare surfaces. In other words, a Na_3PO_4 terminated NZSP surface is more thermodynamically favorable than a bare NZSP surface. The lower energy of the Na_3PO_4 capped surfaces provides a fundamental explanation for the presence of Na_3PO_4 on the surface of $Na_{3.4}Zr_2Si_{2.4}P_{0.6}O_{12}$.

Although the current analysis of Na_3PO_4 surface layers was limited to the $(1\bar{1}02)$ surface, it is likely that the presence of Na_3PO_4 will also have an impact on higher energy surfaces, particularly ones with low Zr coordination. A single monolayer of Na_3PO_4 was also adopted in the current study to limit the computational cost, however the exact thickness of the Na_3PO_4 layer will be the subject of future work.

3.5. Fast-charging capability of NZSP electrolytes

Having demonstrated that the minimization of the Na|NZSP interface resistance is correlated to the *in-situ* formation of a thin layer on the NZSP surface, we now investigate how its presence impacts the cycling performance of NZSP electrolytes. Conventionally, the ability of SEs to withstand high current densities is studied by CCD measurements. Supplementary figure 16 shows such a CCD experiment for a symmetrical cell with a thermally activated NZSP sample subjected to a stepwise increase in current density from 0.5 to 15 mA cm^{-2} at a constant plating/stripping capacity of 0.25 mAh cm^{-2}. The test was conducted at room temperature and without externally applied pressure (other than the wave spring used in the coin cell). A maximum stripping current density of 10 mA cm^{-2} could be reached before a soft short-circuit was

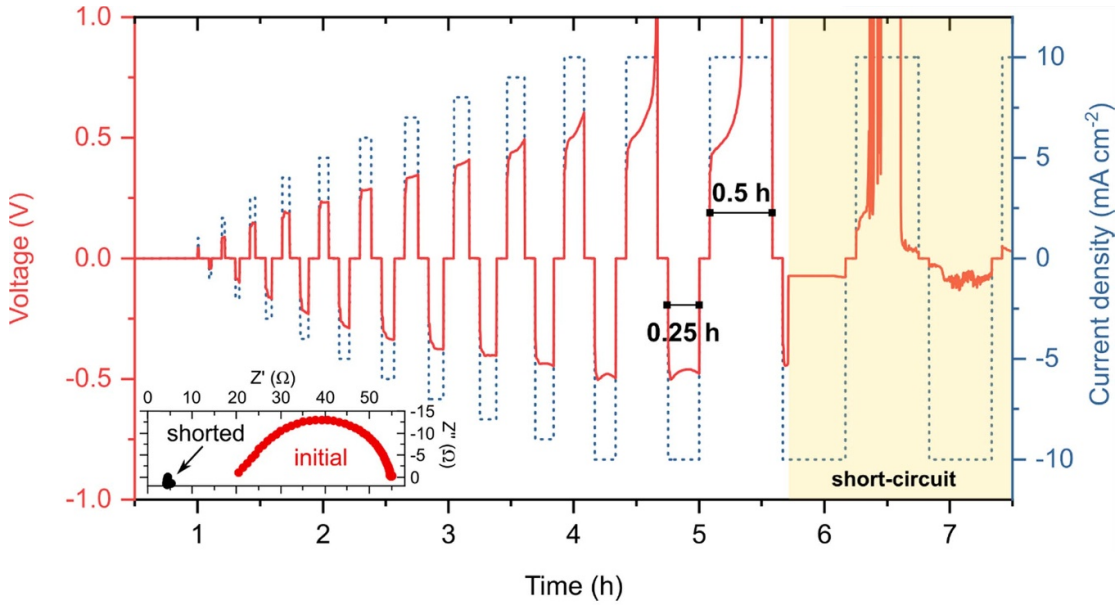

Figure 5. Fast-charging capability of NZSP electrolytes. Voltage profile of a Na|$NZSP_{as\ sintered}$|Na cell subject to a simultaneous increase in current densities (from 1 to 10 mA cm^{-2}) together with an increase in the galvanostatic dwell durations (from 30 s to 0.5 h). Impedance spectra before cycling and after the short-circuit are shown in inset. NZSP pellet thickness: 1.70 mm; Na metal anodes diameter: 8.5 mm; electrode capacities: 11 mAh (equivalent thickness: 182 μm); measured at room temperature.

observed on the next plating cycle (as the two electrodes in symmetrical cells are Na metal, the 'plating' direction was arbitrarily attributed to negative current densities in supplementary figure 16). In contrast, when a finely polished NZSP sample was employed (as in supplementary figure 17 with a $NZSP_{EtOH4000}$ pellet), the CCD was only 0.3 mA cm^{-2} before a soft short-circuit occurred. Previous studies have established that the formation of pores at the metal|SE interface under fast stripping rates are responsible for the nucleation and rapid propagation of dendrites on subsequent plating cycles [20, 22, 26]. The formation of pores at the Na|NZSP interface is suggested by the gradual increase in cell potential over each half-cycle (more clearly observable from 4 mA cm^{-2} onwards in supplementary figure 16). We speculate that the large CCD obtained with thermally activated NZSP can be explained by the good Na wettability of their Na_3PO_4 surface which delays the formation of interfacial pores.

To ensure that NZSP electrolytes will operate at commercially relevant plating/stripping capacities under such high current densities, a solution to delay the apparition of interfacial pores is required. Formation cycles can be used for that purpose as illustrated in figure 5. By gradually increasing the galvanostatic dwell duration at the same time as the current density (which we here call formation cycles), a stable plating of Na metal for 15 min at 10 mA cm^{-2} can be obtained (2.5 mAh cm^{-2} cycled capacity). A stripping cycle for 0.5 h at 10 mA cm^{-2} can even be held although resulting in a large increase in the cell resistance (up to 798 Ω) and in cell failure on the subsequent plating cycle. Considering that this performance was obtained for a planar interface, without any externally applied pressure, and at room temperature, these results predict the high potential of NZSP as a SE for high power application. Strategies enabling the suppression of interfacial pores and extended cycling of NZSP cells will be investigated as part of future work.

4. Discussion

The complex nature of an experimental alkali metal|SE interface creates a challenge for separating the relative contributions of distinct ionically blocking processes. For such interfaces, the interface resistance and charge transfer resistance cannot be confused: while the interface resistance corresponds to the apparent sum of all interface processes with a resistive contribution, the charge transfer resistance only accounts for the resistance associated with the $Na^0_{anode} \leftrightarrow Na^+_{SE} + e^-_{anode}$ conversion across a perfect interface. Hence, charge transfer is only one contribution to the overall interface resistance. In a recent study, Krauskopf *et al* were able to carefully produce a pristine Li|LLZO interface, virtually free from any contamination: an extremely low interface resistance of 0.1 Ω cm^2 at room temperature was measured and attributed to charge transfer across the Li|LLZO interface [37]. With this study, Krauskopf *et al* proved, at least for the Li|LLZO interface, that charge transfer is a marginal contribution to the interface resistance and that all resistive contributions above 0.1 Ω cm^2 should be attributed to other ionically blocking processes.

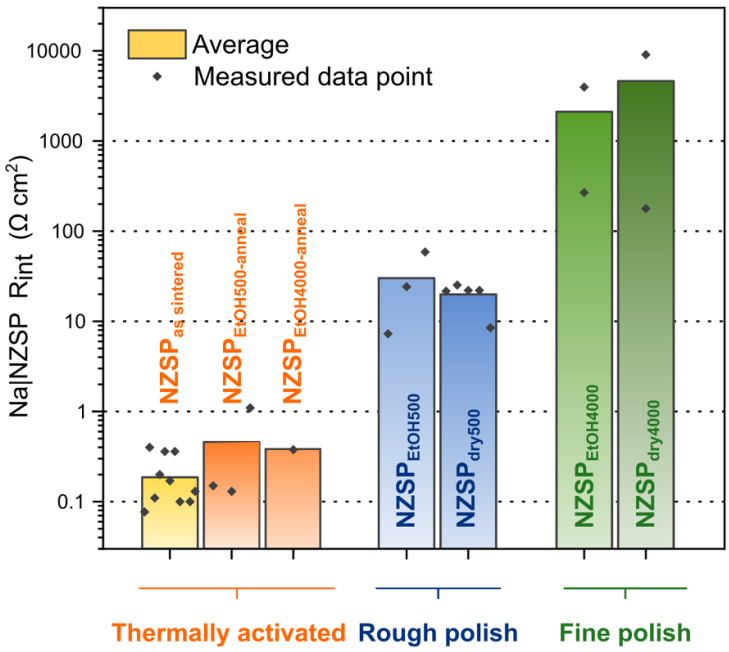

Figure 6. Interface resistances of Na|NZSP|Na symmetrical cells. Bar chart of mean interface resistance values obtained with Na|NZSP|Na symmetrical cells.

Pragmatically, contaminant-free and perfectly wetting interfaces are difficult to prepare and manipulate. Therefore, under more conventional experimental conditions, the akali metal|SE interface resistance is predominantly affected by (a) pores between the metal anode and SE resulting in improper contact [47], (b) adventitious contaminants sandwiched between the anode and the SE (layers formed on the surface of the SE or metal anode by reaction with a gas environment prior to cell assembly) [21, 39–41, 48] or (c) solid electrolyte interphases (SEI, degradation products formed at the interface resulting from the thermodynamic instability of the SE against the metal anode). Regarding adventitious contamination, our results demonstrate that NZSP surfaces are stable even if handled in ambient air (the C signal in figure 2 only accounts for 4 at.% of the total surface signal) in comparison to other oxide SEs such as LLZO or Na-β/β''-alumina [21, 39]. Regarding the electrochemical stability of the Na|NZSP interface, several studies have recently suggested the existence of a rapidly forming SEI [49–52].

With the aim to isolate the contribution of charge transfer from other resistive contributions to the interface resistance, in this study, a uniaxial load of 500 N was systematically applied during cell assembly (not during electrochemical testing) to guarantee an intimate contact between the SE and Na metal and thus minimize constriction resistance effects. The contribution of an SEI to the measured interfacial resistance was mitigated by measuring the cells quickly after cell assembly (typically 30 min after cell assembly). Besides, by measuring the impedance of a symmetrical cell 4 month after its assembly, we demonstrate that the increment of interface resistance can be limited for $NZSP_{\text{as sintered}}$ to 5 Ω cm^2 (supplementary figure 18) which might be attributed to the protective ability of Na_3PO_4 due to its predicted stability against Na metal as predicted by *ab initio* calculation [53].

The normalized interfacial resistances from all symmetrical cells tested in this study are presented in figure 6. This figure illustrates the range of interfacial resistances which can be obtained for the same alkali metal|SE system when the processing of the SE surface is changed. The most striking result is the negligibly low interface resistance which is consistently obtained (the measurement was repeated ten times in the case of $NZSP_{\text{as sintered}}$ for instance) when thermally activated NZSP samples are used in symmetrical cells. Regardless of the processing history of the NZSP sample (polished or not, rough or smooth surface), if the last step of the surface processing is a thermal treatment, a low Na|NZSP interface resistance is obtained.

Combining two surface sensitive techniques (XPS and LEIS), we were able to identify a specific surface termination (Na_3PO_4) common to all thermally activated NZSP samples. The fact that this Na_3PO_4 layer can be sputtered even with a low dose of low energy ions points to a thickness of only a few atomic planes. Although more experiments would be required to confirm this hypothesis, we suggest that the Na_3PO_4 layer may be a form of complexion on the NZSP surface [14, 54–57]. The formation of this surface termination is demonstrated to be thermodynamically favorable by our DFT calculations. Whilst polishing NZSP samples removes this Na_3PO_4 surface termination, a thermal annealing will promote the reconstruction of a Na_3PO_4

surface to minimize surface energy. Whilst our LEIS results and DFT calculations predict that the Na_3PO_4 layer covers the entire NZSP surface uniformly, we associate the presence of larger segregated islands on the surface of $NZSP_{as\ sintered}$ (see supplementary figures S11 and S12) to the slight excess of Na and P used to promote densification during synthesis. These local inhomogeneities in the thickness of the Na_3PO_4 layer do not seem to affect the electrochemical performance of cells. The Na_3PO_4 layer improves adhesion at the Na|NZSP interface as demonstrated by the extremely low Na|NZSP interface resistance and by the non-deviation from ohmic regime during cycling even at high current densities. An important additional benefit of this surface termination is its role as a buffer layer preventing the formation of a resistive SEI at the Na|NZSP interface: unlike other recent studies [52, 58], the increase in interface resistance after four months of cell assembly is only 5 Ω cm^2. The thermodynamic stability of Na_3PO_4 against Na metal [53] could thus be exploited to protect NZSP surfaces.

The order of magnitude difference in interfacial resistance observed between cells employing roughly or finely polished NZSP pellets (figure 6) is attributed to a combination of factors. First, finely polished NZSP surfaces were characterized by a larger presence of contaminants on their surface (see C1s signal of $NZSP_{dry4000}$ and $NZSP_{EtOH4000}$ in supplementary figures 7 and 8). In line with the conclusions from other groups, [21, 39–41, 59] we also observe that adventitious carbon species negatively affect charge transfer at the Na|NZSP interface. Second, the surface chemistry of the Na metal foils used in cells was analyzed by XPS (see supplementary figure S19) and is characterized by the presence of adventitious contaminants even if prepared and handled in a clean glovebox (O_2 and H_2O < 1 ppm) for a few minutes. We suggest that high interface resistances could be the result of this ionically insulating passivation layer on Na metal which rough NZSP surfaces are able to break (upon plastic deformation of Na on NZSP during cell assembly) but not finely polished ones. Third, the surface orientation of NZSP grains on the pellet surface could also have an impact on the efficiency of Na^+ transfer at the Na|NZSP interface: whilst rough polishing may only reveal low energy surfaces because grains are ripped off from the surface, fine polishing cleaves grains revealing potentially different grain orientations with higher energy which could possibly be connected to a higher reactivity and the higher concentration of contaminants observed.

5. Conclusions

Enabling fast-charging SSBs requires to optimize the interface between alkali metal anodes and SEs. In this study, we revealed the existence of a beneficial Na_3PO_4 layer on the surface of NZSP which improves its affinity towards Na metal. We demonstrated that this Na_3PO_4 layer is formed *in-situ* by thermally activating NZSP samples (either by sintering or annealing pellets after polishing). The Na|NZSP interface resistance of cells employing thermally activated NZSP pellets is consistently below 1 Ω cm^2. The ability of thermally activated NZSP samples to withstand high current densities and homogeneously plate Na metal was demonstrated by their CCD of 10 mA cm^{-2}.

Overall, a robust procedure to optimize the Na|NZSP interface is presented. The excellent performance of as-sintered NZSP samples is very promising for industrial prospects because no additional processing steps are required to obtain stable anodic half-cells.

Declaration of interests

The authors declare no competing interests.

Data availability statement

All data that support the findings of this study are included within the article (and any supplementary files).

Acknowledgments

E Q and A A thank Dr Gwilherm Kerherve for his help with the XPS system, and Dr Peter A A Klusener, Dr Samuel J Cooper and Professor Nigel P. Brandon for fruitful discussions. I D S acknowledges the Imperial College Research Computing Service (10.14469/hpc/2232), and associated support services used during this work. This work has been funded by the Engineering and Physical Sciences Research Council (EPSRC/17100026 and EPSRC/R002010/1 Grants), the European Commission (Grant FETPROACT-2018-2020 'HARVERSTORE' 824072) and Shell Global Solutions International B V.

Supplementary information description

Document S1. Supplementary methods, supplementary note 1, figures 1–18, and supplementary tables 1–3

ORCID iD

Ainara Aguadero https://orcid.org/0000-0001-7098-1033

References

[1] Albertus P, Babinec S, Litzelman S and Newman A 2018 Status and challenges in enabling the lithium metal electrode for high-energy and low-cost rechargeable batteries *Nat. Energy* **3** 16–21
[2] Grey C P and Tarascon J M 2016 Sustainability and *in situ* monitoring in battery development *Nat. Mater.* **16** 45–56
[3] Tarascon J M and Armand M 2001 Issues and challenges facing rechargeable lithium batteries *Nature* **414** 359–67
[4] Bieker G, Winter M and Bieker P 2015 Electrochemical *in situ* investigations of SEI and dendrite formation on the lithium metal anode *Phys. Chem. Chem. Phys.* **17** 8670–9
[5] Banza Lubaba Nkulu C *et al* 2018 Sustainability of artisanal mining of cobalt in DR Congo *Nat. Sustain.* **1** 495–504
[6] Frankel T and Whoriskey P 2016 Indigenous people are left poor as tech world takes lithium from under their feet *The Washington Post*
[7] Whoriskey P 2016 China pollution caused by graphite mining for smartphone battery *The Washington Post*
[8] Frankel T 2016 Cobalt mining for lithium ion batteries has a high human cost *The Washington Post*
[9] Larcher D and Tarascon J-M 2014 Towards greener and more sustainable batteries for electrical energy storage *Nat. Chem.* **7** 19–29
[10] Ma Q and Solid-State Electrolyte T F 2020 Materials for sodium batteries: towards practical applications *ChemElectroChem* **7** 2693–713
[11] Goodenough J B, Hong H Y P and Kafalas J A 1976 Fast Na+ ion transport in skeleton structures *Mater. Res. Bull.* **11** 203–20
[12] Hong H P 1976 Crystal structures and crystal chemistry in the system $Na_{1+x}Zr_2SixP_{3-x}O12$ *Mater. Res. Bull.* **11** 173–82
[13] Ma Q *et al* 2019 Room temperature demonstration of a sodium superionic conductor with grain conductivity in excess of 0.01 S cm −1 and its primary applications in symmetric battery cells *J. Mater. Chem.* A **7** 7766–76
[14] Luo J 2019 Let thermodynamics do the interfacial engineering of batteries and solid electrolytes *Energy Storage Mater.* **21** 50–60
[15] Samiee M *et al* 2017 Divalent-doped $Na_3Zr_2Si_2PO_{12}$ natrium superionic conductor: improving the ionic conductivity via simultaneously optimizing the phase and chemistry of the primary and secondary phases *J. Power Sources* **347** 229–37
[16] Okubo K *et al* 2018 A dense NASICON sheet prepared by tape-casting and low temperature sintering *Electrochim. Acta* **278** 176–81
[17] Narayanan S, Reid S, Butler S and Thangadurai V 2019 Sintering temperature, excess sodium, and phosphorous dependencies on morphology and ionic conductivity of NASICON $Na_3Zr_2Si_2PO_{12}$ *Solid State Ion.* **331** 22–29
[18] Shen L, Yang J, Liu G, Avdeev M and Yao X 2021 High ionic conductivity and dendrite-resistant NASICON solid electrolyte for all-solid-state sodium batteries *Mater. Today Energy* **20** 100691
[19] Yang J *et al* 2020 Ultrastable all-solid-state sodium rechargeable batteries *ACS Energy Lett.* **5** 2835–41
[20] Krauskopf T, Richter F H, Zeier W G and Janek J 2020 Physicochemical concepts of the lithium metal anode in solid-state batteries *Chem. Rev.* **120** 7745–94
[21] Sharafi A *et al* 2017 Surface chemistry mechanism of ultra-low interfacial resistance in the solid-state electrolyte Li7La3Zr2O12 *Chem. Mater.* **29** 7961–8
[22] Wang M J, Choudhury R and Sakamoto J 2019 Characterizing the li-solid-electrolyte interface dynamics as a function of stack pressure and current density *Joule* **3** 2165–78
[23] Pesci F M *et al* 2018 Elucidating the role of dopants in the critical current density for dendrite formation in garnet electrolytes *J. Mater. Chem.* A **6** 19817–27
[24] Wang D, Zhu C, Fu Y, Sun X and Yang Y 2020 Interfaces in garnet-based all-solid-state lithium batteries *Adv. Energy Mater.* **10** 2001318
[25] Krauskopf T, Hartmann H, Zeier W G and Janek J 2019 Toward a fundamental understanding of the lithium metal anode in solid-state batteries—an electrochemo-mechanical study on the garnet-type solid electrolyte $Li_{6.25}Al_{0.25}La_3Zr_2O_{12}$ *ACS Appl. Mater. Interfaces* **11** 14463–77
[26] Kasemchainan J *et al* 2019 Critical stripping current leads to dendrite formation on plating in lithium anode solid electrolyte cells *Nat. Mater.* **18** 1105–11
[27] Spencer Jolly D *et al* 2020 Sodium/Na β″ Alumina Interface: effect of Pressure on Voids *ACS Appl. Mater. Interfaces* **12** 678–85
[28] Hitz G T *et al* 2019 High-rate lithium cycling in a scalable trilayer Li-garnet-electrolyte architecture *Mater. Today* **22** 50–57
[29] Pesci F M *et al* 2020 Establishing ultralow activation energies for lithium transport in garnet electrolytes *ACS Appl. Mater. Interfaces* **12** 32806–16
[30] Niehus H, Heiland W and Taglauer E 1993 Low-energy ion scattering at surfaces *Surf. Sci. Rep.* **17** 213–303
[31] Brongersma H H, Draxler M, De Ridder M and Bauer P 2007 Surface composition analysis by low-energy ion scattering *Surf. Sci. Rep.* **62** 63–109
[32] Smets B M J and Lommen T P A 1982 Ion beam effects on glass surfaces *J. Am. Ceram. Soc.* **65** c80–c81
[33] Kresse G and Furthmüller J 1996 Efficient iterative schemes for *ab initio* total-energy calculations using a plane-wave basis set *Phys. Rev.* B **54** 11169–86
[34] Perdew J P, Burke K and Ernzerhof M 1996 Generalized gradient approximation made simple *Phys. Rev. Lett.* **77** 3865–8
[35] Blöchl P E 1994 Projector augmented-wave method *Phys. Rev.* B **50** 17953–79
[36] Ma Q *et al* 2016 Scandium-substituted $Na_3Zr_2(SiO_4)_2(PO_4)$ prepared by a solution-assisted solid-state reaction method as sodium-ion conductors *Chem. Mater.* **28** 4821–8
[37] Krauskopf T *et al* 2020 The fast charge transfer kinetics of the lithium metal anode on the garnet-type solid electrolyte $Li_{6.25}Al_{0.25}La_3Zr_2O_{12}$ *Adv. Energy Mater.* **10** 2000945
[38] Baer D R *et al* 2020 XPS guide: charge neutralization and binding energy referencing for insulating samples *J. Vac. Sci. Technol.* A **38** 031204

[39] Bay M et al 2019 Sodium plating from Na-β″-alumina ceramics at room temperature, paving the way for fast-charging all-solid-state batteries *Adv. Energy Mater.* **10** 1902899
[40] Huo H et al 2020 Li2CO3: a critical issue for developing solid garnet batteries *ACS Energy Lett.* **5** 252–62
[41] Meng J, Zhang Y, Zhou X, Lei M and Li C 2020 Li_2CO_3-affiliative mechanism for air-accessible interface engineering of garnet electrolyte via facile liquid metal painting *Nat. Commun.* **11** 3716
[42] Kramer D and Ceder G 2009 Tailoring the morphology of LiCoO2: a first principles study *Chem. Mater.* **21** 3799–809
[43] Wang L, Zhou F, Meng Y S and Ceder G 2007 First-principles study of surface properties of $LiFePO_4$: surface energy, structure, Wulff shape, and surface redox potential *Phys. Rev.* B **76** 165435
[44] Naqash S, Ma Q, Tietz F and Guillon O 2017 $Na_3Zr_2(SiO_4)_2(PO_4)$ prepared by a solution-assisted solid state reaction *Solid State Ion.* **302** 83–91
[45] Jalalian-Khakshour A et al 2020 Solid-state synthesis of NASICON ($Na_3Zr_2Si_2PO_{12}$) using nanoparticle precursors for optimisation of ionic conductivity *J. Mater. Sci.* **55** 2291–302
[46] Jain A et al 2013 Commentary: the materials project: a materials genome approach to accelerating materials innovation *APL Mater.* **1** 011002
[47] Krauskopf T, Hartmann H, Zeier W G and Janek J 2019 Toward a fundamental understanding of the lithium metal anode in solid-state batteries—an electrochemo-mechanical study on the garnet-type solid electrolyte $Li_{6.25}Al_{0.25}La_3Zr_2O_{12}$ *ACS Appl. Mater. Interfaces* **11** 14463–77
[48] Etxebarria A et al 2020 Work function evolution in li anode processing *Adv. Energy Mater.* **10** 2000520
[49] Yang J et al 2020 Guided-formation of a favorable interface for stabilizing Na metal solid-state batteries *J. Mater. Chem.* A **8** 7828–35
[50] Gao Z et al 2020 Stabilizing Na 3 Zr 2 Si 2 PO 12 /Na interfacial performance by introducing a clean and Na-deficient surface *Chem. Mater.* **32** 3970–9
[51] Gao H, Xin S, Xue L and Goodenough J B 2018 Stabilizing a high-energy-density rechargeable sodium battery with a solid electrolyte *Chem* **4** 833–44
[52] Wang S, Xu H, Li W, Dolocan A and Manthiram A 2018 Interfacial chemistry in solid-state batteries: formation of interphase and its consequences *J. Am. Chem. Soc* **140** 250–7
[53] Lacivita V, Wang Y, Bo S H and Ceder G 2019 *Ab initio* investigation of the stability of electrolyte/electrode interfaces in all-solid-state Na batteries *J. Mater. Chem.* A **7** 8144–55
[54] Kaplan W D, Chatain D, Wynblatt P and Carter W C 2013 A review of wetting versus adsorption, complexions, and related phenomena: the rosetta stone of wetting *J. Mater. Sci.* **48** 5681–717
[55] Naqash S, Sebold D, Tietz F and Guillon O 2019 Microstructure–conductivity relationship of $Na_3Zr_2(SiO_4)_2(PO_4)$ ceramics *J. Am. Ceram. Soc.* **102** 1057–70
[56] Luo J 2015 Interfacial engineering of solid electrolytes *J. Mater.* **1** 22–32
[57] Stegmaier S et al 2021 Nano-scale complexions facilitate li dendrite-free operation in latp solid-state electrolyte *Adv. Energy Mater.* **11** 2100707
[58] Zhang Z et al 2020 $Na_3Zr_2Si_2PO_{12}$: a stable Na+ -ion solid electrolyte for solid-state batteries *ACS Appl. Energy Mater.* **3** 7427–37
[59] Cheng L et al 2014 The origin of high electrolyte-electrode interfacial resistances in lithium cells containing garnet type solid electrolytes *Phys. Chem. Chem. Phys.* **16** 18294–300